

Relationship Between the 3D Porosity and β -Phase Distributions and the Mechanical Properties of a High Pressure Die Cast AZ91 Mg Alloy

SOMJEET BISWAS, FEDERICO SKET, MICHELE CHIUMENTI,
IVÁN GUTIÉRREZ-URRUTIA, JON M. MOLINA-ALDAREGUÍA,
and MARIA TERESA PÉREZ-PRADO

Currently, most magnesium lightweight components are fabricated by casting as this process is cost effective and allows forming parts with complex geometries and weak textures. However, cast microstructures are known to be heterogeneous and contain unpredictable porosity distributions, which give rise to a large variability in the mechanical properties. This work constitutes an attempt to correlate the microstructure and the mechanical behavior of a high pressure die cast (HPDC) Mg AZ91 alloy, aimed at facilitating process optimization. We have built a stairway-shaped die to fabricate alloy sections with different thicknesses and, thus, with a range of microstructures. The grain size distributions and the content of β -phase ($Mg_{17}Al_{12}$) were characterized by optical and electron microscopy techniques as well as by electron backscatter diffraction (EBSD). The bulk porosity distribution was measured by 3D computed X-ray microtomography. It was found that the through-thickness microhardness distribution is mostly related to the local area fraction of the β -phase and to the local area fraction of the pores. We correlate the tensile yield strength to the average pore size and the fracture strength and elongation to the bulk porosity volume fraction. We propose that this empirical approach might be extended to the estimation of mechanical properties in other HPDC Mg alloys.

DOI: 10.1007/s11661-013-1783-y

© The Minerals, Metals & Materials Society and ASM International 2013

I. INTRODUCTION

MAGNESIUM alloys have the lowest density ($<1.8 \text{ g/cm}^3$) of all the structural metals. Increasing their use in automobile and aircraft parts would boost energy efficiency by weight saving. Currently, 90 pct of all Mg parts are fabricated by casting^[1,2] as this is the most cost-efficient process. In particular, most Mg components are produced by high pressure die casting (HPDC) as this process results in finer microstructures and allows the manufacturing of more complex geometries.^[3] Wrought Mg alloys have higher mechanical strength than those produced by conventional casting. However, they exhibit higher mechanical anisotropy, which is detrimental to forming processes. Furthermore, the processing of wrought Mg alloys into their final shape is a complex process that requires several stages.^[4] However, as-cast alloys also exhibit some limitations, in

particular low mechanical performance. This is attributed to the presence of microporosity and microstructural inhomogeneities such as gradients in grain size and phase distribution.^[5-21] Further work is required in order to optimize casting methods and thus improve the quality of magnesium cast parts.

The microstructure of HPDC Mg alloys has been characterized mainly utilizing conventional 2D microscopy techniques.^[21-35] Most studies have been performed in Mg-Al systems, particularly in AZ91 (Mg-9 wt pct Al-1 wt pct Zn), AM60 (Mg-6 wt pct Al-0.5 wt pct Mn), and AM50 (Mg-5 wt pct Al-0.5 wt pct Mn) alloys, as they are relatively cheap, readily castable, and have good mechanical behavior.^[21-31] Some studies have also investigated alloys containing additions of rare earth elements, with improved creep and corrosion resistance.^[31-39] It is now well known that the microstructure of HPDC Mg-Al alloys is formed by α -Mg dendrites, β - $Mg_{17}Al_{12}$ second phases, and Al_8Mn_5 particles. The morphology of the eutectic β - $Mg_{17}Al_{12}$ phase is strongly dependent on the processing conditions.^[24-28,40] HPDC castings are inhomogeneous through the thickness and contain a complex 3D microstructure.^[29,30] In areas close to the surfaces, named skin regions, the microstructure is finer as a consequence of a faster cooling rate due to direct contact with the die, while in the inner volume, or core, the microstructure is coarser. Few works have attempted to characterize the 3D microstructure of Mg HPDC castings. For example, Lee *et al.*^[39,41] utilized serial

SOMJEET BISWAS, Research Associate, FEDERICO SKET, Research Associate, JON M. MOLINA-ALDAREGUÍA and MARIA TERESA PÉREZ-PRADO, Senior Researchers, are with the IMDEA Materials Institute, Calle Eric Kandel, 2, 28906 Getafe, Madrid, Spain. Contact e-mail: somjeetbiswas@gmail.com MICHELE CHIUMENTI, Research Staff, International Center for Numerical Methods in Engineering (CIMNE), Universidad Politécnic de Cataluña, UPC Modulo C1, Campus NorteC/Gran Capitá, s/n, 08034 Barcelona, Spain. IVÁN GUTIÉRREZ-URRUTIA, Group Leader, is with Max Planck Institute for Iron Research, Max Planck Strasse, 1, 40237 Düsseldorf, Germany.

Manuscript submitted December 6, 2012.

Article published online May 17, 2013

sectioning of optical micrographs to visualize and represent the three-dimensional pore morphologies of an AM50 alloy. This allowed observation of the connectivity and the spatial correlations of gas and shrinkage pores in a volume of about $1 \times 10^9 \mu\text{m}^3$. Weiler *et al.*^[42] examined the 3D distribution of pores in an AM60 alloy by X-ray tomography. Nagasekhar *et al.*^[40] have investigated the degree of spatial interconnection of the β -phase particles using focused ion beam tomography. It is thus clear that significant effort is still required to obtain a reliable description of the 3D bulk microstructure in HPDC Mg castings.

Various attempts to relate microstructure to mechanical performance in HPDC Mg castings have been carried out by both experimental and modeling approaches.^[7–19,43–49] Several authors^[15–21,23,39–41,43,45,49] have found that the ductility, the yield strength (σ_Y), and the tensile strength are strongly correlated to the area fraction of porosity in the fracture surfaces, but not to the average porosity volume fraction. This would explain the large scatter in ductility values observed in Mg HPDC alloys. Furthermore, this variability has been observed to decrease with increasing temperature.^[16,44] The yield strength and the UTS decrease as microporosity increases^[7,18] due to the reduction of the load-carrying capacity. The sensitivity of these magnitudes to microporosity increases with grain size. The skin region is reported to have higher local stresses and strain hardening than the interior area.^[19,46,48] This is attributed to a more refined microstructure and a larger fraction of eutectic phases. A recent study by Yang *et al.*^[49] suggested that the core regions yield first, due to the softer nature, and that the skin remains elastic until significantly larger stresses. In-situ SEM mechanical testing by Song *et al.*^[11,12] revealed that fracture initiates at large microvoids and at clusters of micropores in accordance with other studies based on ex-situ testing.^[13–16] A number of investigations have established relations between the mechanical behavior and the section thickness in HPDC Mg castings.^[10,20,51,52] The yield strength, the UTS, and the ductility have been observed to decrease with casting thickness,^[10,20,50,51] both at room and elevated temperatures, reaching a saturation value at thicknesses of approximately 4 mm.^[51] Despite all the efforts invested in this area, studies that succeed in establishing quantitative relations between the 3D bulk microstructural features and the mechanical properties are still lacking.

This paper focuses on the correlation between the microstructure and the mechanical properties of Mg AZ91 alloy processed by HPDC. We attempt to construct a predictive approach to optimize the HPDC process of magnesium alloys. Numerical modeling was used as an accurate tool to predict both the solidification and the cooling processes and to compute the actual solidification times at different locations of the casting. We have performed an exhaustive characterization of the grain size distribution, the fraction of eutectic phases, and the bulk porosity distribution by optical and electron microscopy techniques, electron backscatter diffraction (EBSD), and 3D computed X-ray microtomography. These microstructural parameters are

correlated to microhardness and room temperature mechanical properties.

II. EXPERIMENTAL PROCEDURE

A. Processing by High Pressure Die Casting

High pressure die casting of the AZ91 alloy was carried out in a stairway-shaped die with 5 rectangular steps (50 mm length and 100 mm width) with a thickness of 6.7, 5.7, 4.7, 3.7 and 2.7 mm (Figure 1). The molten material was injected at 993 K (720 °C) at a pressure of 1400 bar in 0.55 seconds using a servo-hydraulic HPDC computer-controlled machine. A detailed analysis of the solidification and cooling processes was carried out numerically looking for an accurate description of the magnitude of both the cooling rates and the solidification times at any point of the specimen. The finite element method was used to solve the integral form of the balance of energy equation complemented by the corresponding boundary condition in terms of heat dissipation (by conduction and radiation) through the surrounding environment.^[52] The heat flux was modeled by the Fourier's law, while the phase change contribution was expressed in terms of the total amount of latent heat released in the liquid-to-solid transformation and the solid fraction evolution (Scheil's rule hypothesis).^[53,54]

B. Microstructure Characterization

Microstructure characterization of the different sections of the HPDC AZ91 cast specimens was carried out through the thickness using several microscopy techniques. The area fractions of the skin and core regions were determined by optical microscopy (OM) using an Olympus BX-51 microscope. Area fractions of second-phase particles were estimated by backscattered electron imaging using an EVO-MA15 Zeiss scanning electron microscope (SEM). Quantitative grain size characterization within section thickness was carried out by electron backscattered diffraction (EBSD) using a 6500 F JEOL field emission gun-scanning electron microscope (FEG-SEM) equipped with a TSL OIM EBSD system at 15 kV acceleration voltage.

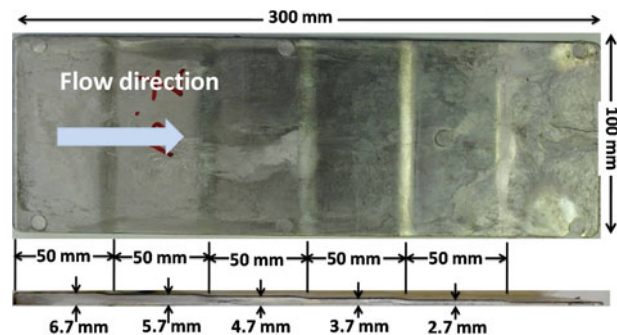


Fig. 1—HPDC AZ91 plate with steps of different thickness.

Sample preparation for microstructure examination was carried out by grinding with different grades of sand papers followed by polishing with 0.5 μm diamond paste to obtain a mirror finish. The surfaces were subsequently etched with a mixture of 75 pct ethanediol, 1 pct HNO_3 , and 24 pct distilled water for ~ 15 seconds at ambient temperature to resolve the phases and grain boundaries. For EBSD examination, colloidal silica polishing was additionally performed in order to obtain a surface finish of less than $\sim 0.05 \mu\text{m}$. A final electrolytic polishing step with the commercial AC2 electrolyte was carried out.

Quantitative information of the 3D porosity distribution in the different sections of the HPDC cast parts was obtained by means of X-ray computed microtomography (XCT). The tomography measurements were performed with a Nanotom 160NF tomograph from Phoenix at 90 to 100 kV and 100 to 160 μA using a tungsten target. 2300 radiographs were acquired for each tomogram with an exposure time of 750 ms. The tomograms were reconstructed using an algorithm based on the filtered back-projection procedure for Feldkamp cone beam geometry. The reconstructed volumes presented a resolution of 4 to 9 μm depending on the sample thickness (Table I). Relatively large volumes were analyzed by tomography in order to obtain relevant statistical data on the porosity inside the material (Table I). The 3D porosity distribution was then analyzed using an in-house-developed MATLAB subroutine in order to obtain the following parameters. First, the maximum and volume-weighted average pore sizes (d_p^{max} and d_p^{avg}) were calculated for all sections of the HPDC AZ91 plate. Second, the porosity volume fraction (f_p^v) was calculated for all the studied sections. Finally, the through-thickness area fraction of the pores (f_p^a) was computed and compared to the through-thickness distributions of microhardness and β -phase area fraction.

C. Mechanical Testing

Microhardness mapping was carried out in a SHIMADZU hardness indenter on a plane containing the through-thickness direction and the metal flow direction in all sections of the cast samples. In order to insure the accuracy of the measurements, hardness measurements were taken at H_V10 . The indentation load was increased until a load-independent hardness value was obtained. At first, indentations were performed along a line parallel to the metal flow direction, each at a

distance of 2 mm. Then, the indenter was shifted by 0.5 mm along the through-thickness direction to obtain further indentations. This was repeated unless the whole thickness of the sample was measured. However, a distance of 1 to 2 mm is always maintained between two indents. Dog bone-type tensile specimens with a gage length of 15 mm were prepared from each section of the HPDC alloy. The thickness of the tensile specimens corresponds to the section thickness of the respective sample. Tensile tests were conducted at an initial strain rate of $5 \times 10^{-4} \text{ s}^{-1}$ in a servo-electric (100 KN) Instron machine. Six tests were carried out for each thickness condition in order to obtain statistically accurate data.

III. RESULTS

A. Local Solidification Time

Figure 2 illustrates the 3D solidification time distribution plot corresponding to the HPDC Mg AZ91 part fabricated for this study, calculated by heat transfer analysis. The solidification time at the core of each section decreases with decreasing thickness, ranging from 3.2 seconds in the 6.7-mm section to 0.7 seconds in the 2.7-mm section. In the 6.7-mm-thick sample, the solidification time corresponding to the skin regions is significantly lower (about 2.8 seconds) than that measured in the core. As the sample thickness decreases, the difference in the solidification time of the skin and the core diminishes.

B. Microstructure

Inspection of a cross-sectional area of all the sections of the HPDC AZ91 plate (ranging in thickness from

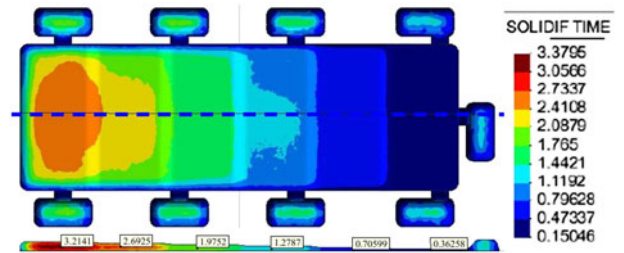


Fig. 2—Color plot showing the solidification time distribution throughout the HPDC AZ91 plate with steps of different thickness.

Table I. Volume Analyzed by XCT, Resolution of XCT Measurements, Average and Maximum Pore Sizes, and Volume Fraction of Pore Present in the Skin, Core, and Full Thickness Corresponding to the Different Thickness Sections of the HPDC AZ91 Plate

Section Thickness (mm)	2.7	3.7	4.7	5.7	6.7
Volume Analyzed by XCT (mm^3)	$2.7 \times 2.7 \times 10$	$3.7 \times 3.7 \times 10$	$4.7 \times 4.7 \times 10$	$5.7 \times 5.7 \times 10$	$6.7 \times 6.7 \times 10$
Resolution of XCT Measurement (μm)	4	5	6	7.5	9
Average Pore Size, d_p^{avg} (μm)	14	17	22	34	32
Maximum Size of Pore, d_p^{max} (μm)	108	155	200	250	247
Volume Fraction of Pores, f_p^v (Pct)					
Core	0.18	0.31	0.11	0.14	0.05
Skin	0.42	0.07	0.27	0.16	0.1
Full Thickness	0.36	0.16	0.2	0.14	0.08

6.7 mm to 2.7 mm) by optical microscopy reveals the presence of three different regions. These are the two skin regions and the core region between them. Figure 3 illustrates the fractions of the sample occupied by the

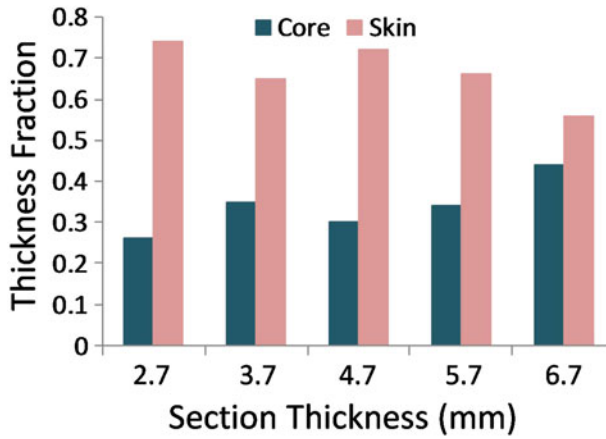


Fig. 3—Bar chart showing the fractions of the total section thickness occupied by the core and by the skin regions.

skin and by the core. It can be seen that in the thinnest section, the skin regions occupy a large fraction of the thickness (~75 pct), whereas in the thickest section, nearly half of the thickness is occupied by the core.

Figure 4 shows five representative optical micrographs per section, taken along a plane containing the through-thickness and metal flow directions. The nature and composition of the phases revealed by OM were further identified by microanalysis in the SEM. The observed microstructure contains α -Mg “islands” (light gray) surrounded by $Mg_{17}Al_{12}$ phase particles (dark gray). Traces of spherically shaped Al_8Mn_5 (γ -phase) particles, 0.5 to 2 μm in size, were also observed throughout the microstructure. This microstructure is consistent with previous reports on HPDC Mg AZ91.^[21–31] The micrographs in Figure 4 also provide qualitative information about the matrix grain size, which is seen to be coarser in the core than in the skin areas. The through-thickness grain size variations are seen to be more pronounced as the section thickness increases. EBSD mapping on the thickest (6.7 mm) and thinnest (2.7 mm) sections along a plane containing the through-thickness and metal flow directions revealed that the thickest section contains larger grains (21 μm in

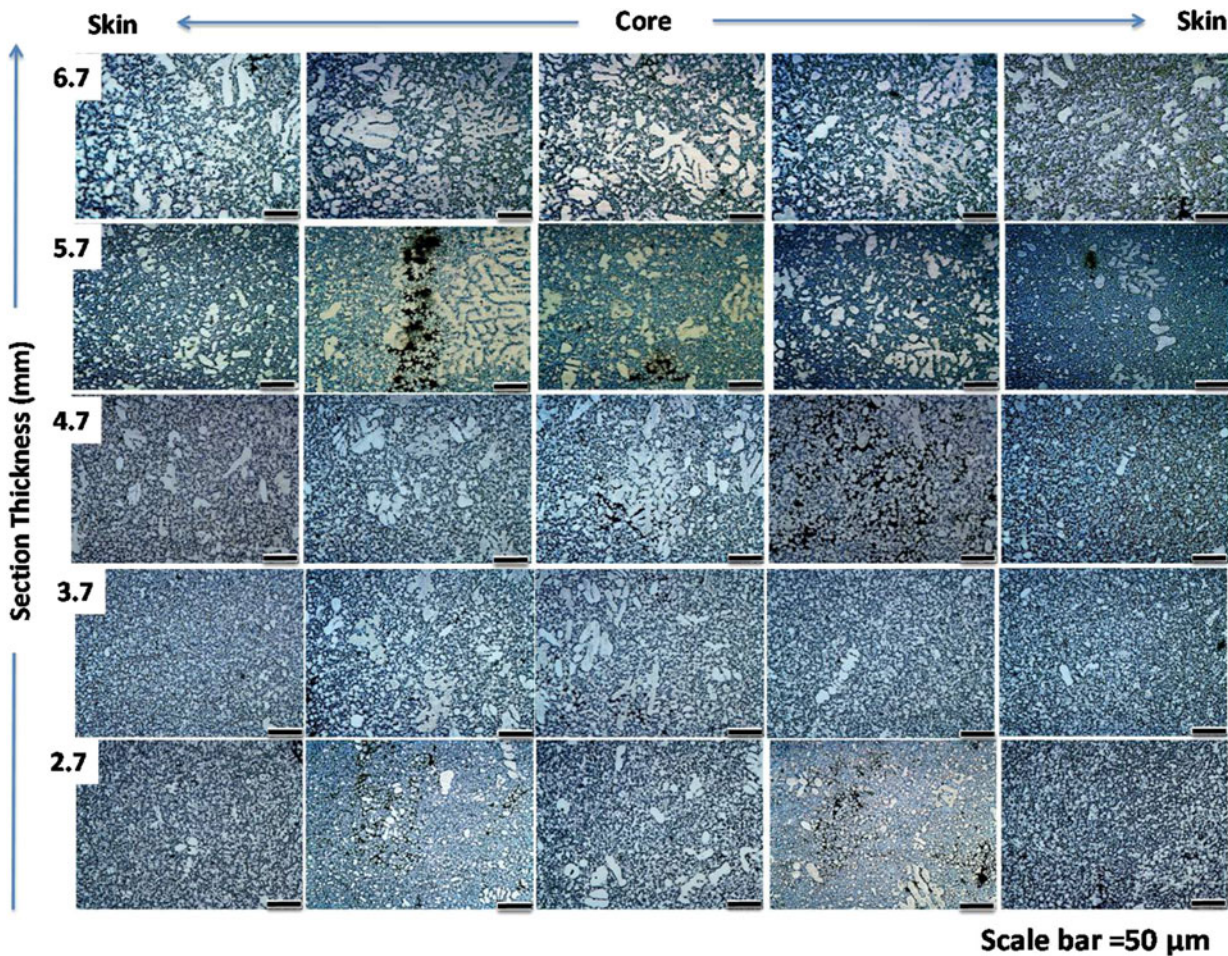


Fig. 4—Optical micrographs illustrating the microstructures along a plane containing the through-thickness and the metal flow directions for the 6.7-, 5.7-, 4.7-, 3.7-, and 2.7-mm-thick sections.

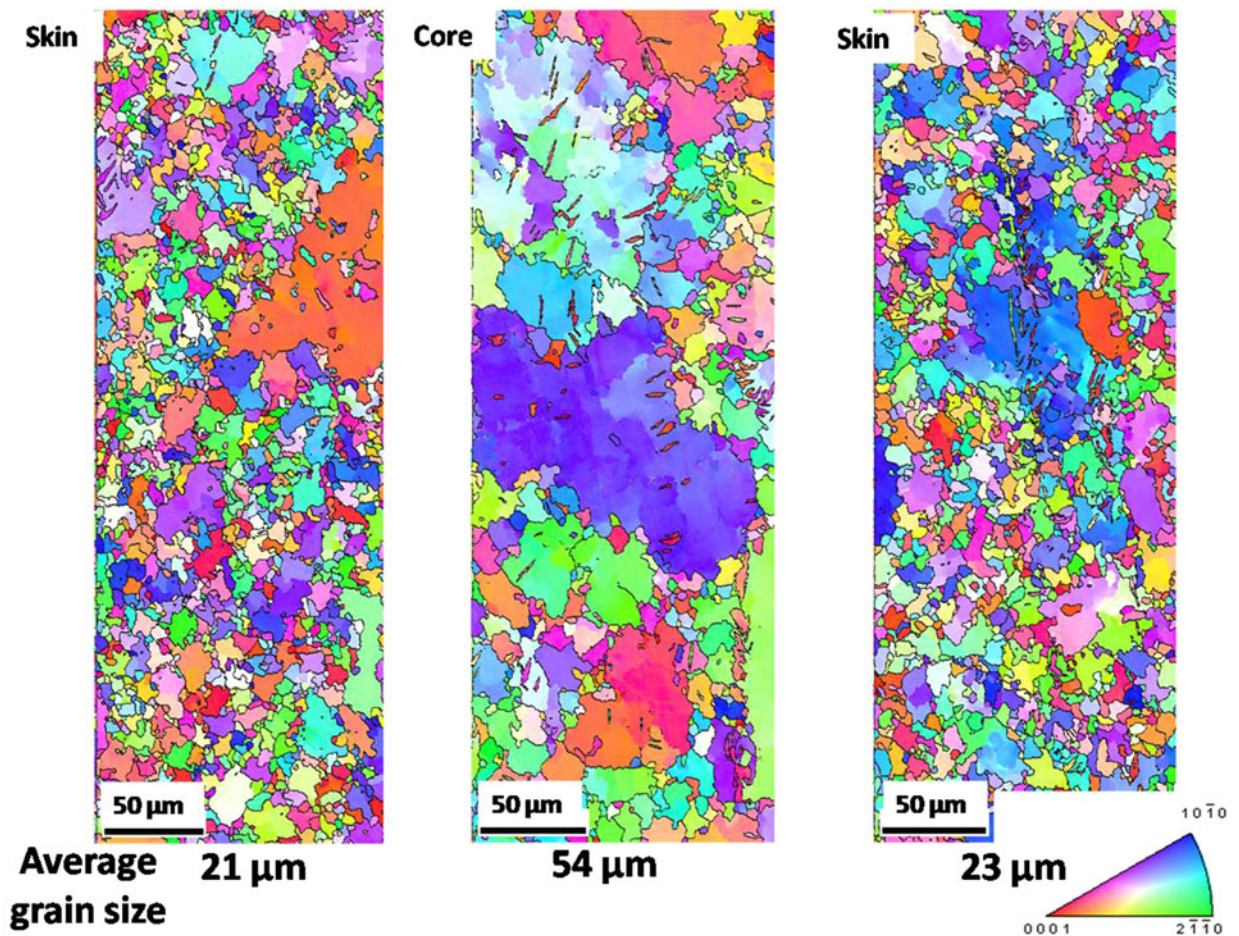


Fig. 5—Inverse pole figure maps corresponding to the skin and core regions of the 6.7-mm-thick section showing the α -Mg grains. Measurements were performed along a plane containing the through-thickness and metal flow directions.

the skin to $54\ \mu\text{m}$ in the core) than the thinnest section ($13\ \mu\text{m}$ in the skin to $15\ \mu\text{m}$ in the core) (Figures 5 and 6). The average grain sizes corresponding to the different regions are also shown in these figures. These results confirm that the grain size is significantly smaller and more homogeneous through the thickness in the 2.7-mm-thick specimen. The grain size distributions corresponding to the same two sections are plotted and compared in Figure 7. It can be seen that in the thickest sample, the distribution is bimodal both in the skin and in the core regions. The microstructure is formed by very coarse grains, typically larger than $60\ \mu\text{m}$, surrounded by finer grains. In the thinnest section, however, the grain size distribution tends to be significantly narrower with few coarse grains smaller than $60\ \mu\text{m}$. The values of the grain size throughout the HPDC AZ91 plate appear to be directly related to the local solidification times (Figure 2).

The spatial distribution of second phases through the thickness of all the sections examined can be qualitatively observed in Figure 4. Second phases are seen to be preferentially located at the boundaries between dendrites and α -Mg “islands.” The area fraction of the $\text{Mg}_{17}\text{Al}_{12}$ (β)-phase was measured through the thickness

of all sections from the backscattered electron SEM images. Figure 8 illustrates the average area fractions of β -phase corresponding to the skin, the core, and the whole section thickness. It can be observed that the area fraction of the β -phase is higher in the skin regions than in the core in all the samples. The average β -phase area fraction corresponding to the whole thickness, weighted taking into account the areas occupied by the skin and the core, is similar in all sections (~ 9.5 pct to 11.5 pct).

The maximum and average pore sizes (d_p^{max} and d_p^{avg}) of the HPDC AZ91 alloy analyzed by XCT are summarized in Table I for all the plate section thicknesses. Both values increase with increasing section thickness. d_p^{max} ranges from $108\ \mu\text{m}$ to $247\ \mu\text{m}$ and the d_p^{avg} ranges from $14\ \mu\text{m}$ to $32\ \mu\text{m}$. The volume fraction of pores (f_p^v) in the core and skin regions and the average value for the whole section thickness are plotted in Figure 9 and summarized in Table I for all the sections under study. In general, f_p^v is higher in the skin regions than in the core and it increases, in all regions, as the section thickness decreases. An exception to this behavior can be found in the 3.7-mm-thick sample. In this particular condition, the volume fraction of the pores in the skin region is very low.

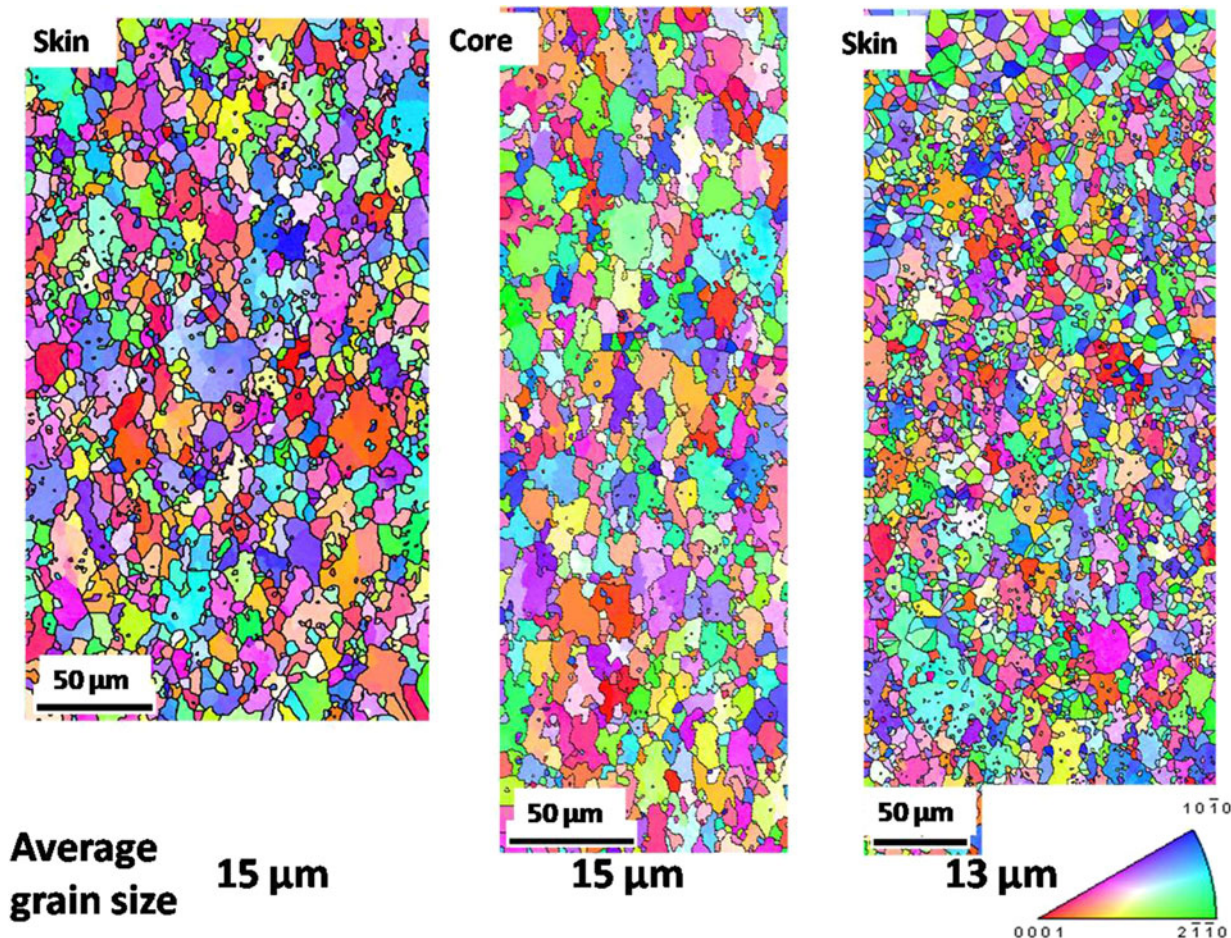


Fig. 6—Inverse pole figure maps corresponding to the skin and core regions of the 2.7-mm-thick section showing the α -Mg grains. Measurements were performed along a plane containing the through-thickness and metal flow directions.

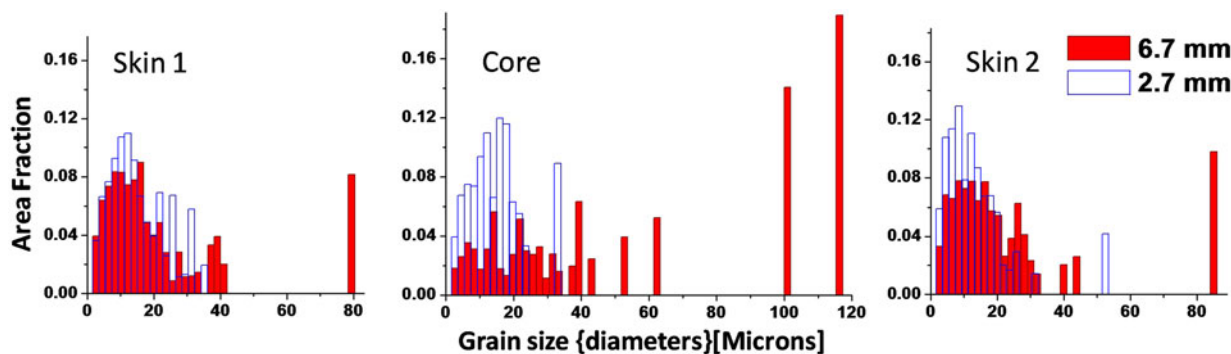


Fig. 7—Grain size distributions corresponding to the skin and core regions of the 6.7-mm and 2.7-mm-thick sections of the α -Mg grains.

C. Mechanical Properties

In Figure 10, the through-thickness distributions of microhardness (Figure 10(a)), area fraction of β -phase ($f_{\beta\text{-phase}}^a$) (Figure 10(b)), and porosity (f_p^a) (Figure 10(c)) are plotted for all the HPDC AZ91 sections. The average hardness is lower in the core than in the skin regions for all the section thicknesses. In almost all the cases, there is a hardness maximum at the skin/core interfaces. The β -phase distributions (Figure 10(b)) are plotted over the projections of the maximum gray level

of the tomographic volumes. The volume projected onto the plane of observation reflects the β -phase distribution through the sample thickness since the β -phase has a slightly higher X-ray absorption coefficient than the α -phase. Therefore, it appears slightly brighter in the reconstructed volumes. The area fraction of the β -phase is lower at the core than at the skin regions. In almost all the cases, the area fraction of the β -phase exhibits maxima at the skin/core interfaces. This is in accordance with previous studies,^[29,55] which reported that Al

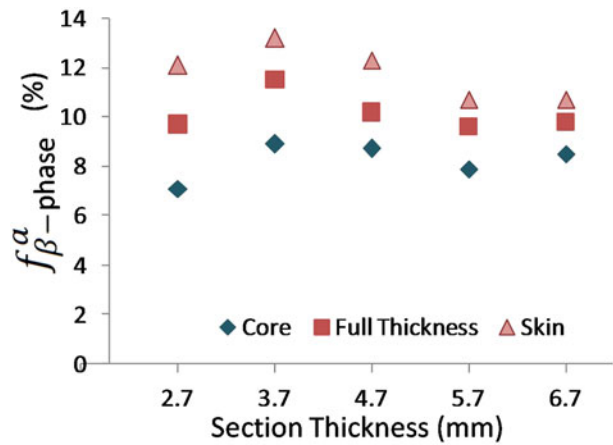


Fig. 8—Average area fraction of the $Mg_{17}Al_{12}$ (β) phase (in pct) in the skin, the core, and the whole section thickness for each section of the HPDC AZ91 alloy.

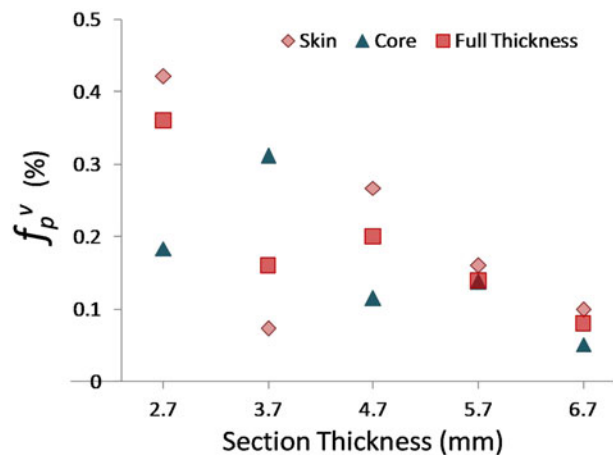


Fig. 9—Volume fraction of porosity (pct) in the skin, the core region, and the whole section thickness for each section of the HPDC AZ91 alloy.

segregation takes place from the pre-solidified core, filling the band between the skin and the core regions and promoting the precipitation of $Mg_{17}Al_{12}$ (β) phase. Good correspondence can be seen between the through-thickness hardness (Figure 10(a)) and β -phase (Figure 10(b)) distributions. The porosity distributions are plotted over the projections of the minimum gray level of the tomographic volumes onto the plane of observation, following a similar procedure as for the β -phase (Figure 10(c)). These projections reflect the porosity distribution through the sample thickness. It can be seen that the skin/core interfaces also contain a large area fraction of pores. Previous works^[19,20,55] have reported that the regions of the skin/core interfaces which cannot be filled with the β -phase are left with shrinkage pores and that gas pores also tend to concentrate there. The presence of a high area fraction of pores at the interfaces results in a local decrease in the value of the hardness, which explains qualitatively the deviations found between the through-thickness

hardness (Figure 10(a)) and β -phase (Figure 10(b)) distributions. The presence of pores further results in an increase in the standard deviation of the hardness.

Figure 10 also reveals that in all the sections of the HPDC AZ91 alloy investigated, the hardness values through the thickness range from about 70 to 80 $kgf\ mm^{-2}$. This suggests that in the present study, the effect of the grain size in the microhardness is small. Thus, the microhardness seems to be related to the β -phase area fraction which is independent of the section thickness. The strong influence of the β -phase on the hardness is justified because this phase is reported to have ~ 1.33 times the hardness of the α -Mg grains.^[56]

Figure 11 shows tensile engineering stress vs strain plots for all the samples investigated. The shape of the curves suggests that premature fracture occurred in all cases. The maximum, average, and minimum values of yield strength (σ_Y), the fracture stress, and the tensile ductility (elongation to fracture, e_F) obtained from all the tensile tests are plotted with respect to the section thickness in Figure 12. σ_Y , as well as its variability, increases with decreasing section thickness. The maximum yield strength of 125 MPa was measured in the 2.7-mm-thick sample. Although the average value of the fracture strength (σ_F) tends to decrease with decreasing thickness, the maximum fracture stress remains almost constant (~ 250 MPa) for thicknesses ranging from 6.7 mm to 3.7 mm. The ductility increases with increasing thickness. A maximum ductility of ~ 18 pct could be observed for the 6.7-mm-thick sample.

IV. DISCUSSION

A. Correlation of the Through-Thickness Distributions of Hardness and β -Phase Area Fraction

Figure 10 reveals that a good correlation exists between the local values of the microhardness and those of the β -phase area fraction ($f_{\beta\text{-phase}}^{\alpha}$) through the thickness of all the studied sections of the HPDC AZ91 alloy. Linear regression analysis was carried out in order to quantify the relationship between these two magnitudes. Figure 13(a) illustrates the experimental data and the fit corresponding to the section with 6.7 mm thickness. Figure 13(b) compares the linear fits corresponding to the other section thicknesses. The corresponding slopes are summarized in a table included as an inset. The analysis reveals that the slope of the linear fit decreases with decreasing thickness. This may be explained as follows. Since β -phase particles are located at α -grain boundaries, in the 6.7-mm-thick sample, these particles are more homogeneously distributed in the skin areas than in the core, as the grain size distribution in the latter is wider (Figure 7). Additionally, in the skin regions, the area fraction of the β -phase is somewhat higher than in the core (Figure 8). Therefore, as observed in Figure 13(b), as the area fraction of the β -phase increases, the spatial distribution of this phase becomes more homogeneous, thus resulting in a hardness profile with the largest difference. However, in the thinnest sample (2.7 mm thickness), the β -phase

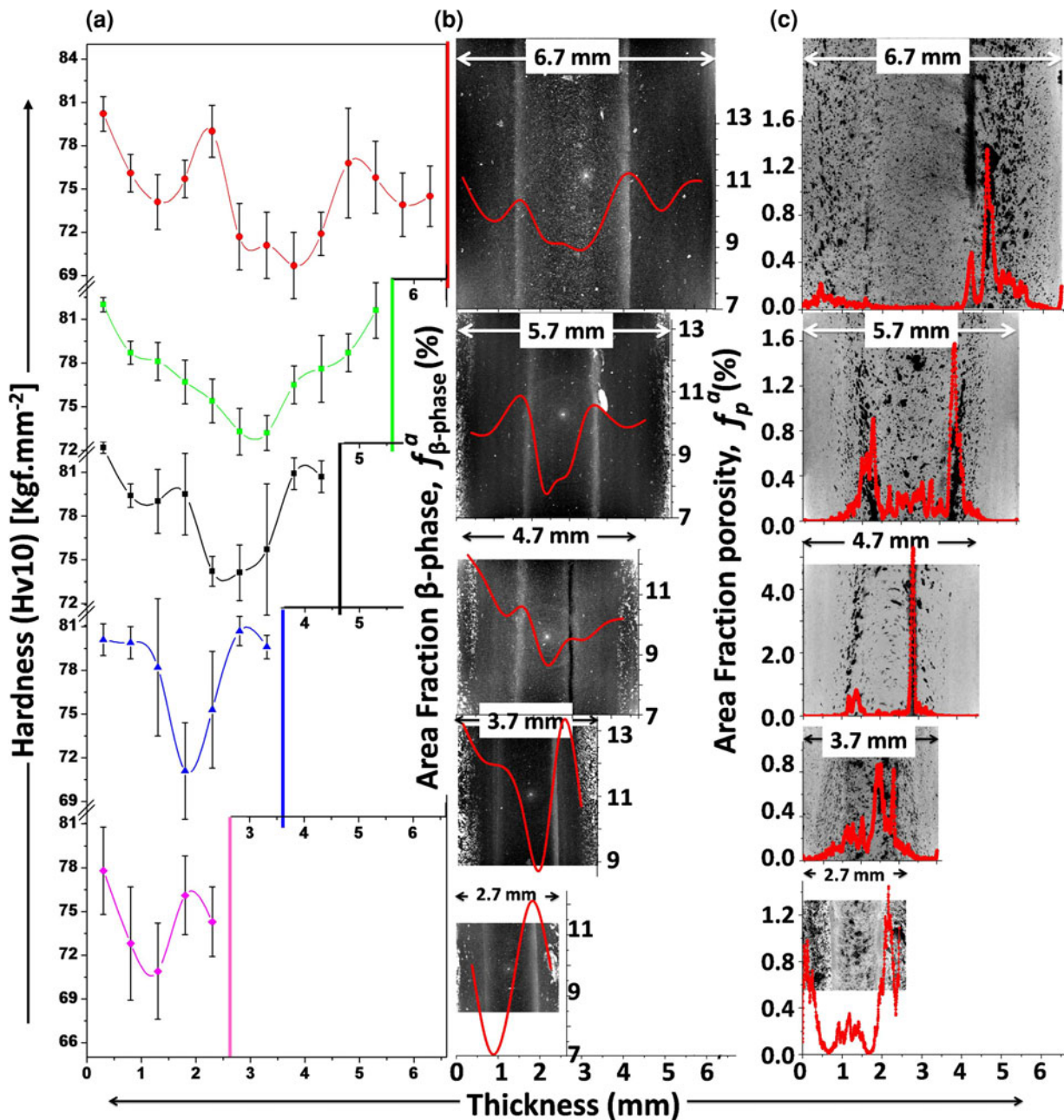


Fig. 10—Comparison of the through-thickness values of the (a) hardness (H_V10), (b) area fraction of β -phase (pct), and (c) area fraction of porosity (pct). (b) is plotted over the projections of the maximum gray level of the tomographic volume reflecting the 3D β -phase distribution through the sample thickness. (c) is plotted over the projections of minimum gray level of the tomographic volume reflecting the 3D porosity distribution through the sample thickness. Darker areas correspond to higher pore fractions.

particles are homogeneously distributed both in the core and in the skin regions due to the presence of similar grain size distributions (Figure 7). Although the difference in area fraction of the β -phase between the core and skin is the largest for this (2.7 mm thick) sample (Figure 8), the variations in the hardness profile are not so pronounced. Hence, the slopes of hardness vs $f_{\beta\text{-phase}}^a$ from Figure 13 seem to be more dependent on the homogeneous grain size distribution throughout the sample thickness than the differences in area fraction of the hardest phase, *i.e.*, the β -phase, for the range of grain sizes and $f_{\beta\text{-phase}}^a$ given in Figures 7 and 8.

B. Correlation of the Bulk Tensile Properties with the Microstructure

In this section, the bulk mechanical properties such as the yield strength, σ_Y , the fracture strength, σ_F , and the elongation to fracture, e_F , will be related to microstructural properties averaged over the entire volume of the samples.

1. Yield stress (σ_Y)

The average σ_Y was observed to increase with decreasing section thickness, ranging from 76 MPa

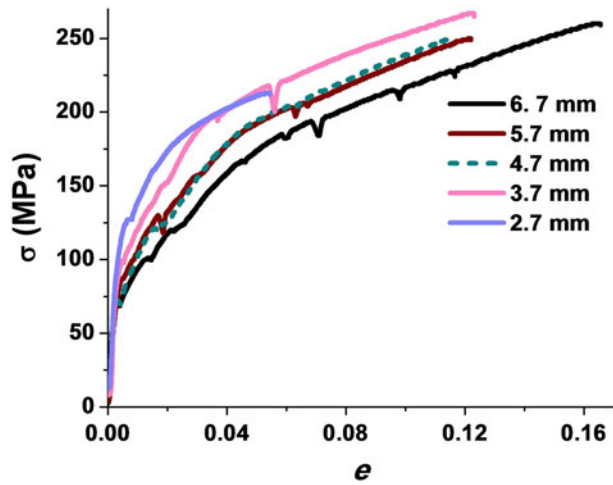


Fig. 11—Engineering stress–strain curves corresponding to the different sections of the HPDC AZ91 Mg plate.

(6.7-mm-thick section) to 100 MPa (2.7-mm-thick section). The grain sizes corresponding to these two samples are $36\ \mu\text{m}$ and $15\ \mu\text{m}$. The grain sizes of the remaining sections are assumed to lie within these two values. Table II summarizes the yield stresses reported in several previous works^[17,57–61] for hot-extruded and gravity-cast HPDC AZ91 samples with the same grain sizes as those belonging to the thickest and thinnest samples. Some values were measured directly and others are extrapolated from the corresponding Hall–Petch plots. The σ_Y values obtained in the present work are similar to those reported for HPDC AZ91,^[17] but significantly smaller, about 2 to 3 times, than those measured in the extruded samples.

It is well known that Mg extrusion textures are usually strong and hence the significantly weak texture of the present HPDC AZ91 alloy might result in a low value of σ_Y . However, we propose that texture weakening alone cannot account for the large difference in yield stresses observed. Recent studies in the anisotropy of the yield strength in extruded Mg–Al alloys have reported maximum σ_Y variations of about 20 pct.^[62] Accordingly, we suggest that the significant mechanical weakening observed in the present work can be mainly associated to the presence of porosity.

As the section thickness decreases, the average pore size, d_p^{avg} , decreases and the volume fraction of pores, f_p^v , increases. A high σ_Y is thus obtained in samples with a high volume fraction of small pores. Figure 14 depicts σ_Y vs d_p^{avg} (Figure 15(a)) and $\text{Ln}(\sigma_Y)$ vs $\text{Ln}(d_p^{\text{avg}})$ (Figure 14(b)) together with the corresponding linear regression plot. It can be seen that the yield stress increases with a decrease in the average pore size. A reasonably good fit was obtained, with $R^2 = 74$ pct and a slope of ~ -0.3 . Thus, the following empirical relation between these two magnitudes is proposed:

$$\sigma_Y = A + B/\sqrt[3]{d_p^{\text{ave}}} \quad [1]$$

where A and B are materials' constants.

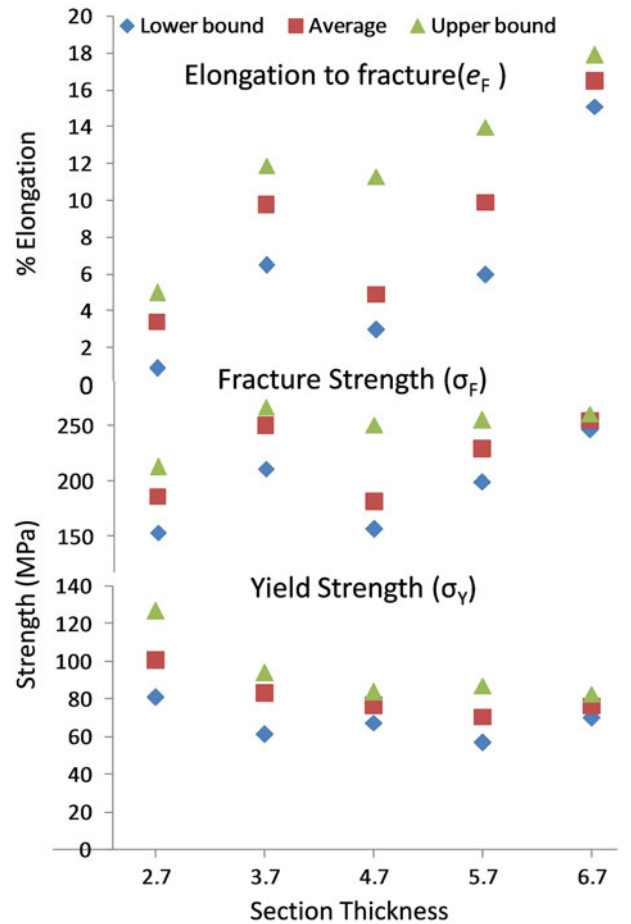


Fig. 12—Variation of the yield strength (σ_Y), the fracture strength (σ_F), and tensile ductility (e_F) with respect to the section thickness of the HPDC AZ91 plate.

The decrease in the yield stress with an increase in d_p^{avg} seems logical as a larger average pore size would result in the presence of a smaller “minimum load bearing area.”

On the other hand, the average distance between the pores, ($d_{\text{pore-pore}}^{\text{avg}}$) and the d_p^{avg} also increases, thus increasing ($d_{\text{pore-pore}}^{\text{avg}}/d_p^{\text{avg}}$) ratio with the increase in section thickness. As the d_p^{avg} is the average size of the pores, and shrinkage pores are considerably complex, the major axis of these pores will be considerably higher than this value. Thus, though the f_p^v is very low (<1 pct), there will be substantial interaction between the pores. Therefore, with the increase in ($d_{\text{pore-pore}}^{\text{avg}}/d_p^{\text{avg}}$), the stress concentration in the pore boundaries increases.^[63] This will also contribute to the decrease in the σ_Y with the increase in the d_p^{avg} .

2. Elongation to fracture (e_F) and fracture stress (σ_F)

In Figure 15, the elongation to fracture (Figure 15(a)) and the fracture stress (Figure 15(b)) are plotted with respect to the volume fraction of pores (f_p^v). It can be seen that both e_F and σ_F are inversely proportional to f_p^v . Figure 16 plots $\text{Ln}(e_F)$ (Figure 16(a)) and $\text{Ln}(\sigma_F)$

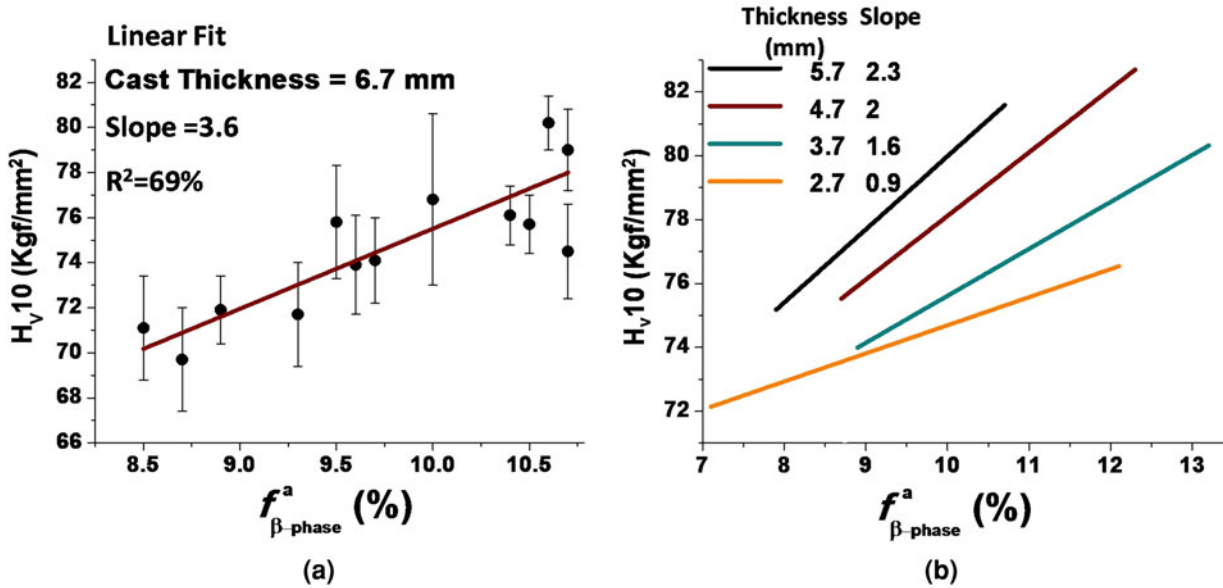


Fig. 13—(a) Experimental hardness (kgf mm^{-2}) values vs the area fraction of β -phase, $f_{\beta\text{-phase}}^a$ (pct), corresponding to the 6.7-mm-thick section and linear regression plot; (b) linear regression plots for all the section thicknesses.

Table II. Summary of the Yield Strength Values Corresponding to the AZ91 Alloy Processed by Wrought and Casting Methods

Grain Size	15 μm	36 μm		
Yield Strength (MPa)	~315	~300	extrusion	Lahaie ^[58]
	275 to 245	~235	extrusion	Mabuchi ^[59]
	~180	~155	extrusion	Nussbaum ^[60]
	~200	~180	ECAP + ext	Chino ^[61]
		~100	gravity die cast + solution treated	Nussbaum ^[62]
	~125	~95	HPDC	Lee ^[17]
	~100	~76	HPDC	present work

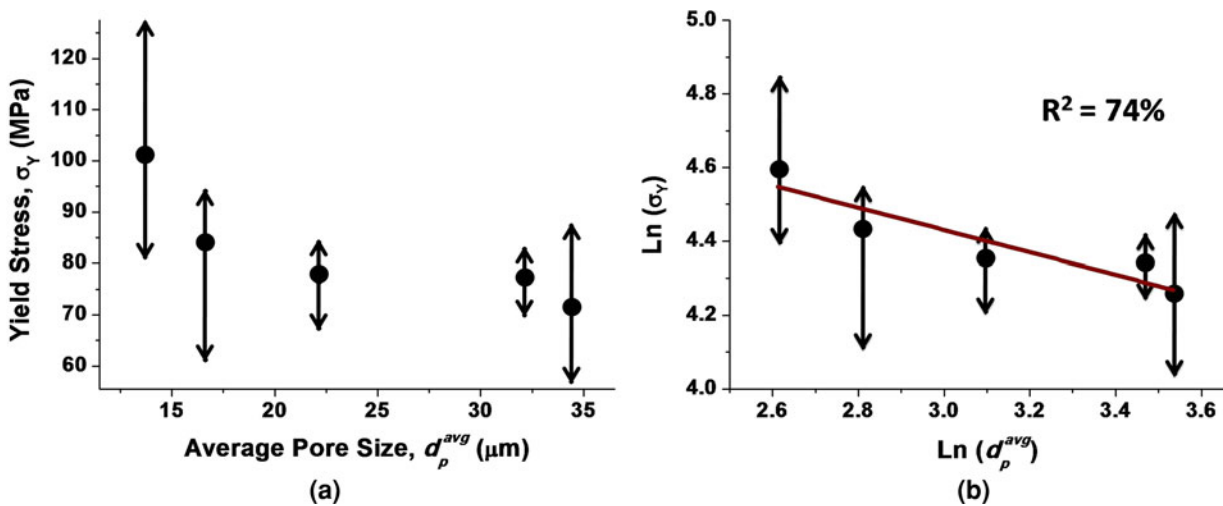


Fig. 14—(a) Yield stress (σ_Y) vs average pore size (d_p^{avg}) plot and (b) $\text{Ln}(\sigma_Y)$ vs $\text{Ln}(d_p^{avg})$ plot.

(Figure 16(b)) vs $\text{Ln}(1 - f_p^v)$. Each graph includes three linear fits corresponding to the maximum, the average, and the minimum values of e_F and σ_F obtained

experimentally from the 6 tensile tests performed for each condition. An excellent correlation ($R^2 > 83$ pct) was obtained between the elongation to fracture and the

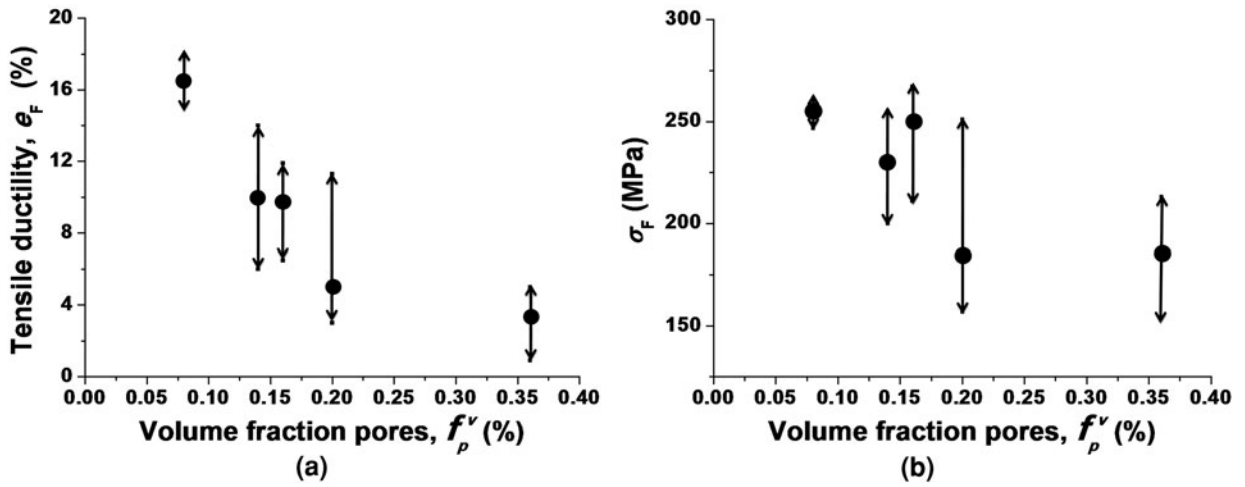


Fig. 15—(a) Tensile ductility and (b) fracture strength (MPa) vs volume fraction of porosity (pct) in the bulk microstructure.

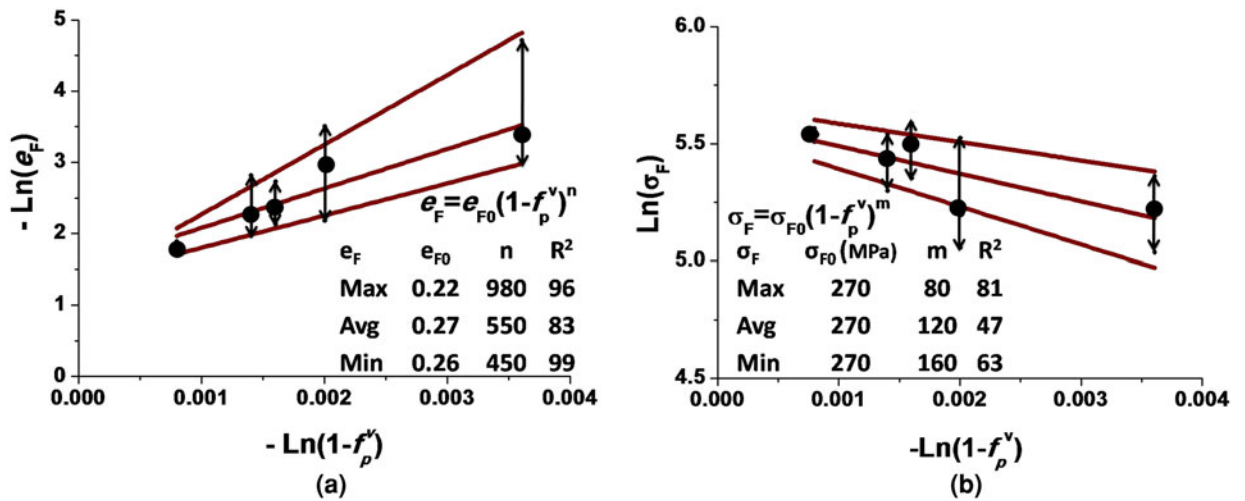


Fig. 16—(a) $-\ln(e_F)$ and (b) $\ln(\sigma_F)$ vs $-\ln(1 - f_p^v)$ plot.

porosity volume fraction (Figure 16(a)). We find the following relationship between these two magnitudes:

$$e_F = e_{F0}(1 - f_p^v)^n \quad [2]$$

The parameters corresponding to the fits are included as an inset in Figure 16(a). The high n exponents obtained ($n > 450$) reveal that a very small increase in the volume fraction of pores will have a dramatic effect on the tensile ductility. When f_p^v tends toward zero, the three fits are seen to converge in a value of approximately 0.25, which would correspond to the elongation to fracture of a pore-free specimen. Figure 16(b) reveals that the fracture stress and the volume fraction of porosity may also be related by the following equation:

$$\sigma_F = \sigma_{F0}(1 - f_p^v)^m \quad [3]$$

The parameters corresponding to the fits are included as an inset in Figure 16(b). Again, the high exponents

obtained suggest that there is a strong dependence of σ_F on f_p^v . However, the m values are significantly smaller than the n exponents. This is consistent with the low strain-hardening capacity of the HPDC AZ91.^[18,20,42] That is, for particular decrease in the porosity volume fraction, the relative increment in the elongation to fracture will be higher than the increment in the fracture stress. When f_p^v tends toward zero, the three fits converge to a value of 270 MPa in a pore-free sample. This value is lower than those reported for extruded pore-free AZ91 alloys^[64,65] due to the weak texture of HPDC castings. Finally, in Figures 16(a) and 16(b), the difference between the upper bound (maximum) fit and the lower bound (minimum) fit increases with f_p^v , which is consistent with an increase in the property variability as the porosity volume fraction increases.

Several authors^[15–18,66] have reported that the elongation to fracture and the fracture stress of HPDC alloys may be related to the area fraction of porosity along the fracture surface. This was justified taking into account the decrease in the load-bearing area by the presence of

pores and considering that the fracture path should preferentially follow the regions containing clusters of pores. The microporosity was estimated from SEM fractography. That approach, thus, allows calculation of the mechanical properties by characterizing the porosity in post-mortem specimens. Other authors^[42] reported that the mechanical properties of HPDC Mg alloys could be correlated with the maximum area fraction of porosity $f_{\text{cross-section}}^{\text{Max area}}$ observed along the gage length of the tensile specimens, which was measured by X-ray tomography with a spatial resolution of 80 μm . Under these conditions, they found a low correlation of the mechanical behavior with the volume fraction of pores. We have developed an empirical approach the novelty of which is that it allows predicting the mechanical properties of HPDC AZ91 from 3D microstructural features such as the average pore size and the volume fraction of porosity, which can be measured from non-destructive tests. Our data suggest additionally that when pores sizes higher than 9 μm are considered, the elongation to fracture and the fracture stress correlate better with the porosity volume fraction than with the area fraction of pores. This work constitutes a step further in the optimization of HPDC processes for Mg alloys. It suggests that for improved mechanical performance, it is critical to reduce the volume fraction of pores and that small reductions in f_p^v can result in dramatic increases of the elongation to fracture and the fracture stress. A reduction of the average pore size also contributes to increasing yield strength values.

V. CONCLUSIONS

An attempt was made to correlate the microstructure and the mechanical properties of a HPDC Mg-9Al-1Zn alloy. With this aim, a step die was designed in order to fabricate specimens with a range of microstructures, which were characterized by optical microscopy, electron backscatter diffraction, scanning electron microscopy, and 3D X-ray computed microtomography (resolution of about 9 μm). The mechanical behavior was characterized by measuring local through-thickness variations of the hardness and bulk tensile properties. The following conclusions can be drawn from the present study:

1. The grain size can be directly related to the solidification time.
2. The average hardness is mainly related to the average content of β -phase and appears to be independent of the grain size.
3. The through-thickness microhardness distribution was seen to be linearly related to the local area fraction of the β -phase. The slope of the linear fit decreases with a reduction in the section thickness due an increase in the homogeneity of the spatial distribution of the β -phase.
4. It is proposed that the yield strength (σ_Y) is related to the average pore size (d_p^{ave}) by the following equation: $\sigma_Y = A + B/\sqrt[3]{d_p^{\text{ave}}}$, where A and B are materials' constants.

5. The elongation to fracture (e_F) and the fracture stress (σ_F) have been correlated to the porosity volume fraction (f_p^v).

ACKNOWLEDGMENTS

The authors would like to thank the vehicle interior manufacturer, Grupo Antolin Ingeniería, S.A., within the framework of the project MAGNO2008-1028-CENIT, funded by the Spanish Ministry of Science and Innovation. Funding under programs PRI-PIBUS-2011-0917 and ESTRUMAT-S2009/MAT-1585 (Madrid Regional Government) is also greatly appreciated. We are grateful to Profs. A. Rollet and L. Tóth for prolific discussions.

REFERENCES

1. K.U. Kainer and F.V. Buch: in *Magnesium Alloys and Technology*, K.U. Kainer, ed., Wiley-VCH Pub. DGM, Weinheim, 2003, p. 9.
2. B.L. Mordike and P. Lukáč: in *Magnesium Technology Metallurgy, Design Data, Applications*, H.E. Friedrich and B.L. Mordike, eds., Springer, Berlin, 2006, pp. 63–107.
3. B.L. Mordike and T. Elbert: *Mater. Sci. Eng. A*, 2001 vol. 302, pp. 37–45.
4. S. Biswas, S.S. Dhinwal, and S. Suwas: *Acta Mater.*, 2010, vol. 58, pp. 3247–61.
5. A. Balasundaram and A.M. Gokhale: *Mater. Character.*, 2001, vol. 46, p. 419.
6. A.K. Dahl, S. Sannes, D.H. St. John, and H. Westengen: *J. Light Metals*, 2001, vol. 1, p. 9.
7. J.P. Weiler and T.J. Wood: *Mater. Sci. Eng. A*, 2009, vol. 527, pp. 25–31.
8. D.G.L. Prakash, D. Regener, and W.J.J. Vorster: *Mater. Sci. Eng. A*, 2008, vol. 488, pp. 303–310.
9. D.G.L. Prakash, D. Regener, and W.J.J. Vorster: *J. Alloys Compd.*, 2009, vol. 470, pp. 111–16.
10. H. Hu, M. Zhou, Z. Sun, and N. Li: *J. Mater. Proc. Technol.*, 2008, vol. 2, pp. 364–68.
11. J. Song, S.-M. Xiong, M. Li, and J. Allison: *J. Alloys Compd.*, 2009, vol. 477, pp. 863–69.
12. J. Song, S.-M. Xiong, M. Li, and J. Allison: *Mater. Sci. Eng. A*, 2009, vol. 520, pp. 197–201.
13. Y. Lu, F. Taheri, and M. Gharghour: *J. Alloys Compd.*, 2008, vol. 466, pp. 214–27.
14. Y. Lu, F. Taheri, M. Gharghour, and H.P. Han: *J. Alloys Compd.*, 2009, vol. 470, pp. 202–213.
15. S.G. Lee, G.R. Patel, A.M. Gokhale, A. Sreeranganathan, and M.F. Horstemeyer: *Mater. Sci. Eng. A*, 2006, vol. 427, pp. 255–62.
16. S.G. Lee, G.R. Patel, A.M. Gokhale, A. Sreeranganathan, and M.F. Horstemeyer: *Scripta Mater.*, 2005, vol. 53, pp. 851–56.
17. C.D. Lee: *Mater. Sci. Eng. A*, 2007, vol. 459, pp. 355–60.
18. C.D. Lee: *Mater. Sci. Eng. A*, 2007, vols. 454–455, pp. 575–80.
19. C.H. Cáceres, J.R. Griffiths, A.R. Pakdel, and C.J. Davidson: *Mater. Sci. Eng. A*, 2005, vol. 402, pp. 258–68.
20. C.H. Cáceres, W.J. Poole, A.L. Bowles, and C.J. Davidson: *Mater. Sci. Eng. A*, 2005, vol. 402, pp. 269–77.
21. S.G. Lee and A.M. Gokhale: *Scripta Mater.*, 2006, vol. 55, pp. 387–90.
22. S. Otarawanna, C.M. Gourlay, H.I. Laukli, and A.K. Dahle: *Mater. Character.*, 2009, vol. 60, pp. 1432–41.
23. S.G. Lee, G.R. Patel, and A.M. Gokhale: *Mater. Character.*, 2005, vol. 55, pp. 219–24.
24. S. Barbagallo, H.I. Laukli, O. Lohne, and E. Cerri: *J. Alloys Compd.*, 2004, vol. 378, pp. 226–32.
25. D.G.L. Prakash and D. Regener: *J. Alloys Compd.*, 2008, vol. 461, pp. 139–46.

26. D.G.L. Prakash and D. Regener: *J. Alloys Compd.*, 2009, vol. 467, pp. 271–77.
27. M.S. Dargusch, M. Nave, S.D. McDonald, and D.H. St. John: *J. Alloys Compd.*, 2010, vol. 492, pp. 64–68.
28. M. Wu and S. Xiong: *J. Mater. Sci. Technol.*, 2011, vol. 27, pp. 1150–56.
29. J.P. Weiler, J.T. Wood, R.J. Klassen, R. Berkmortel, and G. Wang: *Mater. Sci. Eng. A*, 2006, vol. 419, pp. 297–305.
30. L. Hu, S. Chen, Y. Miao, and Q. Meng: *Appl. Surf. Sci.*, 2012, doi:10.1016/j.apsusc.2012.08.116.
31. L. Shepeleva and M. Bamberger: *Mater. Sci. Eng. A*, 2006, vol. 425, pp. 312–17.
32. M.S. Dargusch, S.M. Zhu, J.F. Nie, and T.L. Dunlop: *Scripta Mater.*, 2009, vol. 60, pp. 116–19.
33. I.P. Moreno, T.K. Nandy, J.W. Jones, J.E. Allison, and T.M. Pollock: *Scripta Mater.*, 2001, vol. 45, pp. 1423–29.
34. W. Xiao, S. Zhu, M.A. Easton, M.S. Dargusch, M.A. Gibson, and J.F. Nie: *Mater. Charact.*, 2012, vol. 65, pp. 28–36.
35. W. Xiao, M.A. Easton, M.S. Dargusch, S. Zhu, and M.A. Gibson: *Mater. Sci. Eng. A*, 2012, vol. 539, pp. 177–84.
36. S.M. Zhu, M.A. Gibson, M.A. Easton, and J.F. Nie: *Scripta Mater.*, 2010, vol. 63, pp. 698–703.
37. F. Mert, C. Blawert, K.U. Kainer, and N. Hort: *Corrosion Sci.*, 2012, doi:<http://dx.doi.org/10.1016/j.corsci.2012.08.011>.
38. J. Zhang, M. Zhang, J. Meng, R. Wu, and D. Tan: *Mater. Sci. Eng. A*, 2010, vol. 527, pp. 2527–37.
39. S.G. Lee and A.M. Gokhale: *Scripta Mater.*, 2007, vol. 56, pp. 501–04.
40. A.V. Nagasekhar, C.H. Cáceres, and C. Kong: *Mater. Charact.*, 2010, vol. 61, pp. 1035–42.
41. S.G. Lee, A.M. Gokhale, and A. Sreeranganathan: *Mater. Sci. Eng. A*, 2006, vol. 427, pp. 92–98.
42. J.P. Weiler, T.J. Wood, R.J. Klassen, E. Maire, R. Berkmortel, and G. Wang: *Mater. Sci. Eng. A*, 2005, vol. 395, pp. 315–22.
43. C.H. Cáceres, C.J. Davidson, J.R. Griffiths, and C.L. Newton: *Mater. Sci. Eng. A*, 2002, vol. 325, pp. 344–55.
44. E. Cerri, P. Leo, and P.P. De Marco: *J. Mater. Proc. Technol.*, 2007, vol. 189, pp. 97–106.
45. S.G. Lee, G.R. Patel, and A.M. Gokhale: *Scripta Mater.*, 2005, vol. 52, pp. 1063–68.
46. Z. Shan and A.M. Gokhale: *Mater. Sci. Eng. A*, 2003, vol. 361, pp. 267–74.
47. E. Aghion, N. Moscovitch, and A. Arnon: *Mater. Sci. Eng. A*, 2007, vol. 447, pp. 341–46.
48. D.G.L. Prakash, D. Regener, and W.J.J. Vorster: *Comput. Mater. Sci.*, 2008, vol. 43, pp. 759–66.
49. K.V. Yang, C.H. Cáceres, A.V. Nagasekhar, and M.A. Easton: *Mater. Sci. Eng. A*, 2012, vol. 542, pp. 49–55.
50. M.S. Dargusch, M.A. Easton, S.M. Zhu, and G. Wang: *Mater. Sci. Eng. A*, 2009, vol. 523, pp. 282–88.
51. G. Gu, S. Lin, Y. Xia, and Q. Zhou: *Mater. Des.*, 2012, vol. 38, pp. 124–32.
52. M. Chiumenti, C. Agelet de Saracibar, and M. Cervera: *J. Heat Transf.*, 2008, vol. 130, pp. 1–10.
53. C. Agelet de Saracibar, M. Cervera, and M. Chiumenti: *Int. J. Plasticity*, 1999, vol. 15, pp. 1–34.
54. M. Cervera, C. Agelet de Saracibar, and M. Chiumenti: *Int. J. Numer. Methods Eng.*, 1999, vol. 46, pp. 1575–91.
55. A.K. Dahle, S. Sannes, D.H. St. John, and H. Westengen: *J. Light Met.*, vol. 2001, pp. 99–103.
56. X.-S. Wang and J.H. Fang: *J. Mater. Sci.*, 2004, vol. 39, pp. 2617–20.
57. D. Lahaie, J.D. Embury, M.M. Chadwich, and G.T. Gray: *Scripta Metall.*, 1992, vol. 27, pp. 139–42.
58. M. Mabuchi, K. Hubota, and K. Higashi: *Mater. Trans. JIM*, 1995, vol. 36, pp. 1249–54.
59. G. Nussbaum, P. Sainfort, and G. Regazzoni: *Scripta Metall.*, 1989, vol. 23, pp. 1079–84.
60. Y. Chino and M. Mabuchi: *Adv. Eng. Mater.*, 2001, vol. 3, pp. 981–83.
61. G. Nussbaum, P. Bridot, T.J. Warner, J. Charbonnier, and G. Regazzoni: *Magnesium Alloys and Their Applications*, B.L. Mordike and F. Hehmann, eds., DGM, Germany, 1992, pp. 351–58.
62. S.-B. Yi, C.H.J. Davies, H.-G. Brokmeier, R.E. Bolmaro, K.U. Kainer, and J. Homeyer: *Acta Mater.*, 2006, vol. 54, pp. 549–62.
63. T.L. Anderson: *Fracture Mechanics Fundamentals and Applications*, CRC Press, Boca Raton, FL, 1994, pp. 34, 279.
64. D.M. Lee, B.K. Suh, B.G. Kim, J.S. Lee, and C.H. Lee: *Mater. Sci. Technol.*, 1997, vol. 13, pp. 590–95.
65. H. Ding, L. Liu, S. Kamado, W. Ding, and Y. Kojima: *J. Alloys Compd.*, 2008, vol. 456, pp. 400–06.
66. C.H. Cáceres and B.I. Selling: *Mater. Sci. Eng.*, 1996, vol. 220, pp. 109–116.